



NiSn bimetallic nanoparticles as stable electrocatalysts for methanol oxidation reaction

Junshan Li^{a,b,1}, Zhishan Luo^{a,1}, Yong Zuo^{a,b}, Junfeng Liu^{a,b}, Ting Zhang^c, Pengyi Tang^c, Jordi Arbiol^{c,e}, Jordi Llorca^d, Andreu Cabot^{a,e,*}

^a Catalonia Institute for Energy Research – IREC, Sant Adrià del Besòs, Barcelona 08930, Spain

^b Departament d'Electronica, Universitat de Barcelona, 08028 Barcelona, Spain

^c Catalan Institute of Nanoscience and Nanotechnology (ICN2), CSIC and BIST, Campus UAB, Bellaterra, 08193 Barcelona, Spain

^d Institute of Energy Technologies, Department of Chemical Engineering and Barcelona Research Center in Multiscale Science and Engineering, Universitat Politècnica de Catalunya, EEBC, 08019 Barcelona, Spain

^e ICREA, Pg. Lluís Companys 23, 08010 Barcelona, Spain

ARTICLE INFO

Keywords:

Electrocatalysis
Methanol oxidation
Colloidal synthesis
Bimetallic nanoparticles

ABSTRACT

Nickel is an excellent alternative catalyst to high cost Pt and Pt-group metals as anode material in direct methanol fuel cells. However, nickel presents a relatively low stability under operation conditions, even in alkaline media. In this work, a synthetic route to produce bimetallic NiSn nanoparticles (NPs) with tuned composition is presented. Through co-reduction of the two metals in the presence of appropriate surfactants, 3–5 nm NiSn NPs with tuned Ni/Sn ratios were produced. Such NPs were subsequently supported on carbon black and tested for methanol electro-oxidation in alkaline media. Among the different stoichiometries tested, the most Ni-rich alloy exhibited the highest electrocatalytic activity, with mass current density of 820 mA mg^{−1} at 0.70 V (vs. Hg/HgO). While this activity was comparable to that of pure nickel NPs, NiSn alloys showed highly improved stabilities over periods of 10,000 s at 0.70 V. We hypothesize this experimental fact to be associated to the collaborative oxidation of the byproducts of methanol which poison the Ni surface or to the prevention of the tight adsorption of these species on the Ni surface by modifying its surface chemistry or electronic density of states.

1. Introduction

Fuel cells have raised increasing interest as a high efficiency and environmental friendly energy conversion technology. Among the different cell architectures and fuels proposed, direct methanol fuel cells (DMFCs) are the best positioned toward widespread commercialization and the most viable alternative to lithium-ion batteries for portable applications [1,2]. Methanol provides numerous advantages as a fuel, including safe handling, storage and transportation, solubility in aqueous electrolytes, availability and potential generation from renewable energies, high power and energy density (6100 Wh kg^{−1}) with high oxidation rates that do not require C–C bond breaking, low emissions and fast recharging and cell startup at low temperature [3,4]. However, a major drawback of this technology, currently delaying its extensive commercialization, is its high manufacturing cost, which is in large part related to the dependence on Pt-based electrocatalysts for both methanol oxidation at the anode and oxygen reduction at the cathode

[1,5,6]. The development of Pt-free electrocatalysts is thus a key challenge to be urgently overcome for DMFCs to become cost-effective.

Nickel, a relatively abundant element in the earth's crust, is among the best candidate materials to replace Pt in the anode, where the methanol oxidation reaction (MOR) takes place. Ni [7–10] and Ni-based alloys reported to date, such as NiCu [11–14], NiFe [15], NiCo [16], NiMn [17] and NiTi [18,19] show excellent catalytic activities, but even in alkaline electrolytes, they lack of a satisfactory durability. Therefore, the exploration of novel Ni-based compounds presenting improved stabilities is required.

Among the possible alternative alloys, NiSn is a potentially excellent candidate for the MOR. Actually, Sn has been demonstrated to improve Pt performance in this reaction [20–22]. However, surprisingly, NiSn has yet to be tested as anode material in DMFCs. This anomaly is in part associated to the lack of reliable synthetic routes to produce NiSn alloys. Among the very few examples in the literature, Liu et al. produced porous Ni₃Sn₂ intermetallic microcages through a solvothermal method

* Corresponding author at: Catalonia Institute for Energy Research – IREC, Sant Adrià del Besòs, Barcelona 08930, Spain.

E-mail address: acabot@irec.cat (A. Cabot).

¹ These authors contributed equally to this work.

which were tested for lithium and sodium storage [23]. Recently, Liu et al. reported a colloidal synthesis approach that made use of a strong Brønsted base, *n*-butyllithium, to produce Ni_3Sn_2 NPs for the semi-hydrogenation of alkynes [24].

To overcome these challenges, we present here a new synthetic route to produce NiSn NPs with controlled stoichiometry. We further demonstrate these NPs to show high electrocatalytic activities towards methanol electrooxidation and at the same time significantly improved stabilities when compared with nickel.

2. Experimental section

2.1. Chemicals

Nickel(II) acetylacetonate ($\text{Ni}(\text{acac})_2 \cdot x\text{H}_2\text{O}$ ($x \sim 2$), 95%, Sigma-Aldrich), tin(II) acetate ($\text{Sn}(\text{oac})_2$, 95%, Fluka), tri-*n*-octylphosphine (TOP, 97%, Strem), oleylamine (OAm, 80–90%, TCI), borane tert-butylamine complex (TBAB, 97%, Sigma-Aldrich), oleic acid (OAc, Sigma-Aldrich), hydrazine monohydrate (N_2H_4 64–65%, reagent grade, 98%, Sigma-Aldrich), Nafion (10 wt. %, perfluorinated ion-exchange resin, dispersion in water), methanol (anhydrous, 99.8%, Sigma-Aldrich), carbon black (CB, VULCAN XC72), potassium hydroxide (KOH, 85%, Sigma-Aldrich), acetonitrile (CH_3CN , extra dry, Fisher), trioctylphosphine oxide (TOPO, 99%, Sigma-Aldrich), diisobutylaluminum hydride solution (DIBAH, 1.0 M in tetrahydrofuran (THF), Aldrich), tin(II) chloride (SnCl_2 , anhydrous, 98%, Strem), and lithium bis(trimethylsilyl)amide ($\text{LiN}(\text{SiMe}_3)_2$, 97%, Aldrich) were used as received without any further purification. Chloroform, hexane, acetone, toluene, and ethanol were of analytical grade and purchased from various sources. MilliQ water was obtained from a PURELAB flex from ELGA. All the syntheses were performed using standard airless techniques: a vacuum/dry argon gas Schlenk line was used for the synthesis and an argon-filled glove-box was used for storing and dealing with sensitive chemicals.

2.2. Synthesis of NiSn NPs

In a typical synthesis, 7 ml OAm, 0.1 mmol $\text{Ni}(\text{acac})_2$, 0.1 mmol $\text{Sn}(\text{oac})_2$ and 0.15 ml OAc were loaded into a 25 ml three-necked flask and degassed under vacuum at 80 °C for 1 h while being strongly stirred using a magnetic bar. Afterward, a gentle flow of argon was introduced, and 1 ml of TOP was injected into the solution. Subsequently, the reaction flask was heated to 180 °C within 20 min, followed by quick injection of a solution containing 1 mmol TBAB in 1 ml degassed OAm. A visible color change, from light blue to black was observed immediately. The reaction was maintained at this temperature for 1 h before it was quenched using a water bath. NiSn NPs were collected by centrifuging and washing the solid product with acetone and chloroform 3 times. The as-prepared NPs were finally dispersed in chloroform and stored for their posterior use. NPs were colloidally stable in chloroform for over two months. Different nominal Ni/Sn ratios were used to prepare NPs with different stoichiometries following the same procedure above detailed.

2.3. Synthesis of Sn NPs

13 nm Sn NPs were produced according to the method developed by Kravchyk et al. [25]. Briefly, 16 ml OAm was loaded into a 25 ml three-necked flask and maintained under vacuum at 140 °C for 60 min under stirring. After cooling to 50 °C, 0.5 mmol SnCl_2 was added to the flask and kept under vacuum at 140 °C for 30 min. Then temperature was increased to 180 °C under argon and 2 ml of toluene containing 0.6 g of $\text{LiN}(\text{SiMe}_3)_2$ was injected. Immediately afterward, 0.6 ml of a 1 M DIBAH solution in THF was also injected. Upon injection of DIBAH, the solution immediately turned dark brown. After 10 min reaction, the solution was cooled down using a water bath. Acetone was added to the

final mixture and NPs were collected by centrifugation. The obtained precipitate was re-dispersed in hexane for further use.

2.4. Synthesis of Ni NPs

12 nm fcc-Ni NPs were prepared following the procedure described by Chen et al. [26]. In a typical synthesis, 1 mmol $\text{Ni}(\text{acac})_2$, 7 ml OAm, 0.4 mmol TOP and 0.25 mmol TOPO were loaded in a three-neck flask and stirred under a gentle flow of argon. Temperature was raised to 130 °C and kept for 20 min. Then, the solution was quickly heated to 215 °C and maintained at this temperature for 45 min. Subsequently, the flask was cooled down to room temperature using a water bath. The black precipitate was separated through centrifugation after adding ethanol. NPs were re-dispersed and precipitated three times using hexane and ethanol as solvent and non-solvent, respectively. The product was finally dispersed in hexane.

2.5. Ligand removal

NiSn, Sn and Ni NPs dispersed in chloroform were precipitated through addition of ethanol and centrifugation. Then, they were dispersed in a mixture containing 28 ml acetonitrile and 0.8 ml hydrazine hydrate and stirred for 4 h. NPs were then collected by centrifugation and washed with acetonitrile for 3 times. Finally, the NiSn NPs were dried under vacuum.

2.6. Characterization

Powder X-ray diffraction (XRD) patterns were recorded from the as-synthesized NPs dropped on a Si(501) substrate on a Bruker AXS D8 Advance X-ray diffractometer with Ni-filtered (2 μm thickness) Cu K radiation (1.5106) operating at 40 kV and 40 mA. Specimens for transmission electron microscopy (TEM) characterization were prepared by drop casting the dispersions of NPs onto a 200 mesh Cu grids with ultrathin carbon and formvar support films. TEM analyses were carried out on a ZEISS LIBRA 120, operating at 120 kV. High-resolution TEM (HRTEM) and scanning TEM (STEM) studies were carried out using a field emission gun FEI Tecnai F20 microscope at 200 kV with a point-to-point resolution of 0.19 nm. High angle annular dark-field (HAADF) STEM was combined with electron energy loss spectroscopy (EELS) in the Tecnai microscope by using a GATAN QUANTUM filter. The composition of NPs was confirmed by scanning electron microscopy (SEM) on a ZEISS Auriga SEM with an energy dispersive X-ray spectroscopy (EDS) detector at 20 kV. Values were averaged from 3 measurements of each composition. X-ray photoelectron spectroscopy (XPS) was done on a SPECS system equipped with an Al anode XR50 source operating at 150 mW and a Phoibos 150 MCD-9 detector. The pressure in the analysis chamber was kept below 10^{-7} Pa. The area analyzed was about 2 mm \times 2 mm. The pass energy of the hemispherical analyzer was set at 25 eV and the energy step was maintained at 1.0 eV. Data processing was performed with the Casa XPS program (Casa Software Ltd., UK). Binding energies were shifted according to the reference C 1s peak that was located at 284.8 eV. Fourier transform infrared spectrometer (FTIR) data were recorded on an Alpha Bruker FTIR spectrometer with a platinum attenuated total reflectance (ATR) single reflection module.

2.7. Electrochemical characterization

Electrochemical measurements were carried out at room temperature (25 ± 2 °C) in an electrochemical workstation (AutoLab, Metrohm). The three electrode system consisted of a counter electrode (Pt mesh), a working electrode (glassy carbon (GC) electrode with diameter of 5 mm) and a reference electrode (Hg/HgO). The Hg/HgO was placed in a salt bridge of 1.0 M KOH. 5 mg of NPs, 50 μL of 10 wt% Nafion solution together with 10 mg of CB were added to 1 ml ethanol

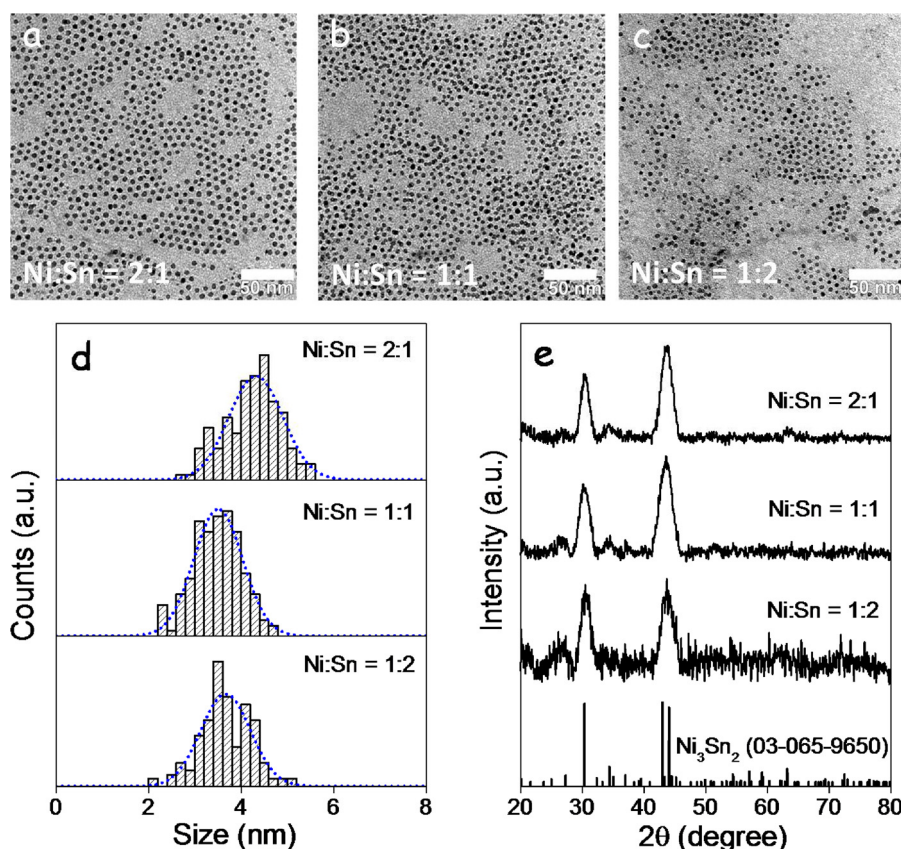


Fig. 1. (a–c) Representative TEM micrographs of NiSn NPs with different nominal Ni:Sn ratios: 2:1 (a); 1:1 (b); and 1:2 (c). (d) Corresponding size distribution histograms. (e) XRD patterns of NiSn NPs with the same nominal stoichiometries.

and 1 ml MilliQ water which was vigorously sonicated for 1 h to obtain a homogeneous solution. Then, 5 μ L of the freshly prepared ink (around 0.012 mg catalyst) was evenly loaded onto the polished glassy carbon electrode and dried naturally in air at room temperature. All the measurements were performed in N₂-bubbled 0.50 M KOH solution in the absence or presence of variable concentrations of methanol with magnetic bar stirring, except where noted. Current densities were calculated taking into account the geometric surface area of the GC electrode (0.196 cm^2).

3. Results and discussion

A co-reduction strategy was developed to produce NiSn NPs with low size dispersion and tuned composition (see experimental section for details). Briefly, proper amounts of Ni(acac)₂ and Sn(oac)₂ were reduced at 180 °C and in the presence of OAc, OAm and TOP by injection of a TBAB/OAm solution. Fig. 1a–c shows representative TEM macrographs of the quasi-spherical NiSn NPs produced with three different nominal Ni:Sn ratios (2:1; 1:1; 1:2). The average size of the NPs measured by TEM analysis fluctuated in the range from $3.5 \pm 0.5 \text{ nm}$ to $4.2 \pm 0.6 \text{ nm}$, depending on the nominal composition (Fig. 1d and Table 1). Fig. 1e displays the XRD patterns of the NiSn NPs produced following the above detailed procedure. As corresponding to small NPs, XRD patterns from all samples displayed broad diffraction peaks, which could be ascribed to the orthorhombic Ni₃Sn₂ or the monoclinic Ni₃Sn₄ crystal phases. Additional Ni₃Sn or even Ni or Sn phases could not be discarded from the XRD analysis. Previous works already reported the formation of these phases in the composition range here analyzed, 33–67% of each metal [27,28].

Extensive HRTEM and EELS analysis found all NiSn NPs to contain both elements, Ni and Sn, in a similar ratio within each sample. No independent Ni or Sn elemental NP was identified in any of the samples

Table 1

Average particle size measured from TEM micrographs, summary of the atomic ratios of Ni to Sn nominally introduced and experimentally measured from EDX and XPS analysis, and ratio of the chemical states obtained from XPS measurements.

Catalysts	TEM average NP size (nm)	Ni/Sn molar ratio			Chemical states (XPS)	
		Nominal	EDX	XPS	Ni(0)/Ni(II)	Sn(0)/Sn(IV)
NiSn-2:1	4.2 ± 0.6	2	1.7	0.41	0.14	0.28
NiSn-1:1	3.5 ± 0.5	1	1.1	0.20	0.20	0.19
NiSn-1:2	3.7 ± 0.5	0.5	0.46	0.10	0.27	0.29

analyzed. Fig. 2a shows HRTEM micrographs of the NiSn (2:1) NPs that had been exposed to air. NiSn NPs had average sizes of ca. 7.2 nm and displayed a core-shell structure. The core, with a diameter of ca. 3.5 nm, was crystalline and its structure matched that of a Ni₃Sn₂ orthorhombic phase (space group = Pnma) with $a = 7.110 \text{ \AA}$, $b = 5.210 \text{ \AA}$, $c = 8.230 \text{ \AA}$ (Fig. 2a). The shell was amorphous and it was attributed to an oxide layer formed during the NP exposure to the ambient atmosphere. STEM-HAADF micrographs and EELS chemical compositional maps revealed the NiSn (2:1) core to be Ni-rich and the shell to be Sn-rich (Fig. 2b). The same crystal phase and compositional organization was observed for NiSn (1:1) NPs. This composition inhomogeneity could be created during the synthesis due to a differential reduction rate of the two precursors, or during oxidation, being Sn atoms potentially more prone to react with ambient oxygen.

EDX analysis showed the composition on the NiSn NPs to match relatively well with the nominal Ni/Sn ratios (Table 1 and Fig. S4). Specifically Ni/Sn ratios of 1.7, 1.1 and 0.46 were obtained for NiSn NPs produced with nominal Ni:Sn stoichiometries 2:1; 1:1 and 1:2,

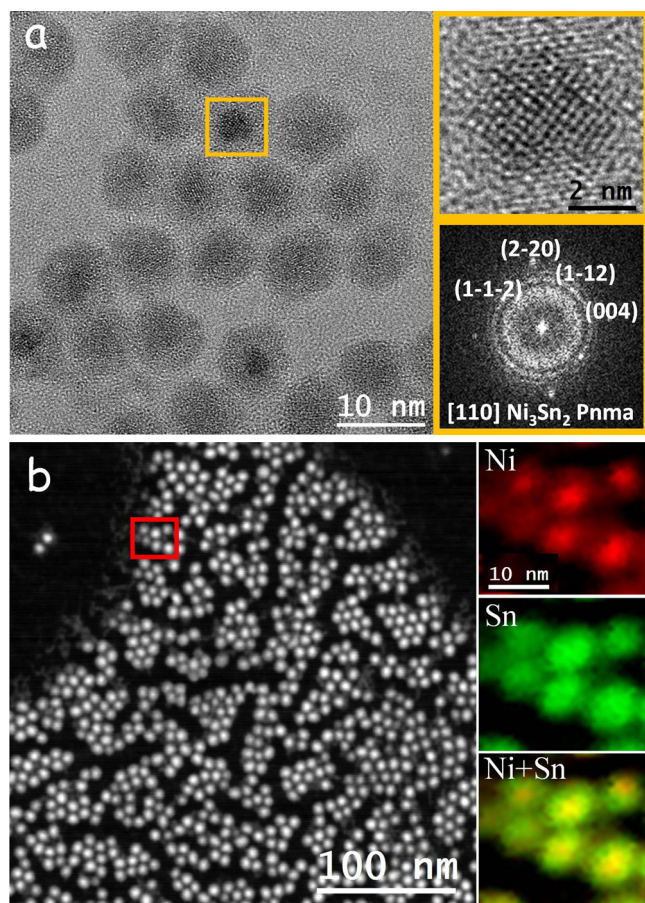


Fig. 2. (a) HRTEM micrograph of NiSn (2:1) NPs and detail of the yellow squared region with its corresponding power spectrum. Ni_3Sn_2 lattice fringe distances measured were 0.210 nm (2–20), 0.296 nm (–1–12) at 46° vs (2–20) and 0.204 nm (004) at 90° vs (2–20), which matched with the orthorhombic Ni_3Sn_2 phase visualized along its [110] zone axis. (b) STEM-HAADF micrographs and EELS elemental maps of several NiSn (2:1) NPs showing a Ni and Sn radial gradient. (For interpretation of the references to colour in this figure legend, the reader is referred to the web version of this article).

respectively.

XPS analysis was used to characterize the chemical environment of atoms at the surface of NiSn NCs that had been exposed to the ambient atmosphere. For these analyses, purified NiSn NPs with no surface ligands were used (see below for ligand removal details). XPS analysis confirmed the surface of these NPs to be Sn-rich and oxidized (Fig. 3).

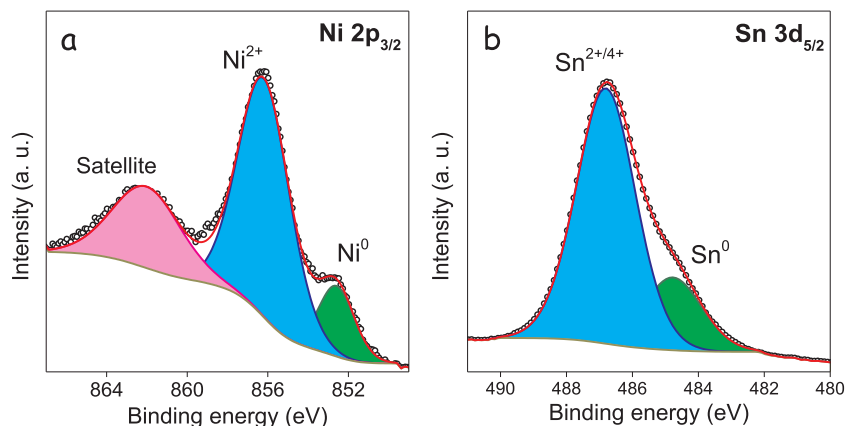


Fig. 3. XPS spectra of the Ni 2P_{3/2} region (a) and of the Sn 3P_{5/2} region (b) of NiSn (2:1) NPs.

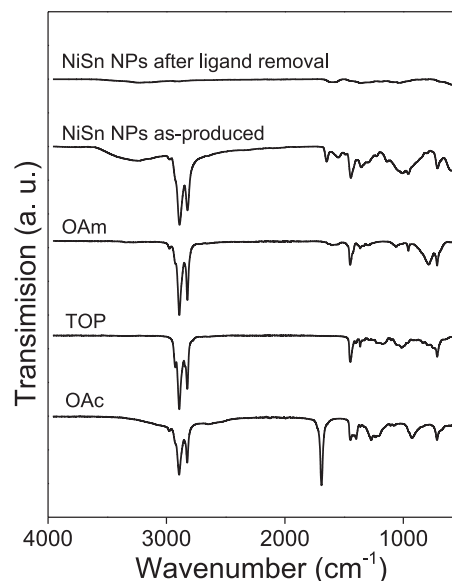


Fig. 4. FTIR spectra of OAm, OAc, TOP and NiSn (2:1) NPs as produced and after ligand removal.

The surface Ni/Sn ratios were 0.41, 0.20 and 0.10 for NiSn NPs produced with nominal Ni:Sn stoichiometries 2:1; 1:1 and 1:2, respectively. Ni 2p_{3/2} electronic states were found at binding energies of 856.3 eV, corresponding to a Ni²⁺ chemical environment, and 852.6 eV, which was associated to a Ni⁰ state [29]. The Ni²⁺ oxidized component was clearly majoritarian, with a ratio over Ni⁰: Ni⁰/Ni²⁺ = 0.14 for the NiSn (2:1) sample. Similar ratios were obtained for NiSn NPs with other Ni/Sn nominal compositions, with an increase of the Ni⁰ component with the Sn ratio (see Table 1). The main contribution to the Sn 3d_{5/2} electronic states were found at a binding energy of 486.8 eV, which was attributed to a Sn²⁺ or Sn⁴⁺ chemical environment [29]. A minor component was found at 484.7 eV, which was associated to metallic Sn. The ratio of the two chemical states was Sn⁰/Sn^{2+/4+} = 0.28 for the NiSn (2:1) NPs and fluctuated with the nominal composition of the samples (Table 1). This fluctuation may be associated to a different amount of time the samples were exposed to air before XPS analysis. Sn was more strongly affected by this experimental parameter as the NPs surface was rich in Sn and poor in Ni. Probably, the relative amount of Ni on the NP surface also decreased when increasing the Sn composition.

The presence of OAm, OAc and TOP in the reaction mixture was essential to produce monodisperse and colloidally stable NiSn NPs with the orthorhombic Ni_3Sn_2 crystal phase. Keeping all the synthetic

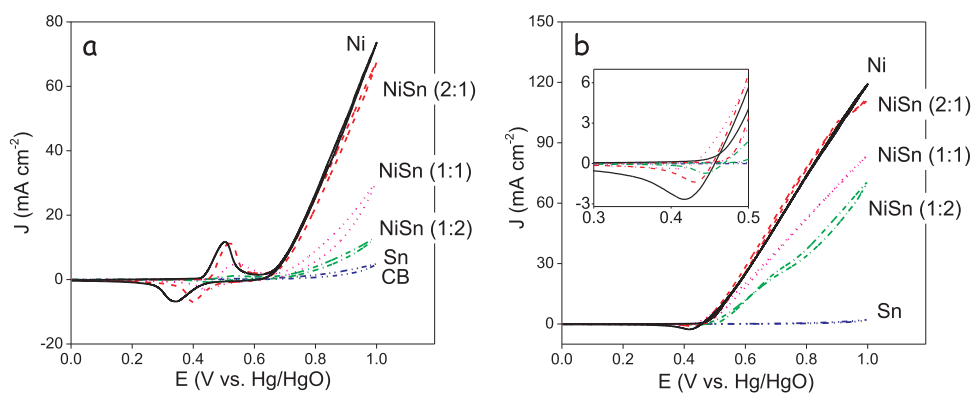


Fig. 5. (a) Cyclic voltammograms of Ni-Sn, Ni, Sn NPs in 0.50 M KOH solution at a scan rate of 50 mV s⁻¹. (b) Cyclic voltammograms of NiSn NPs, Ni NPs and Sn NPs for methanol electrooxidation in 0.50 M KOH containing 0.50 M methanol solution at a scan rate of 50 mV s⁻¹.

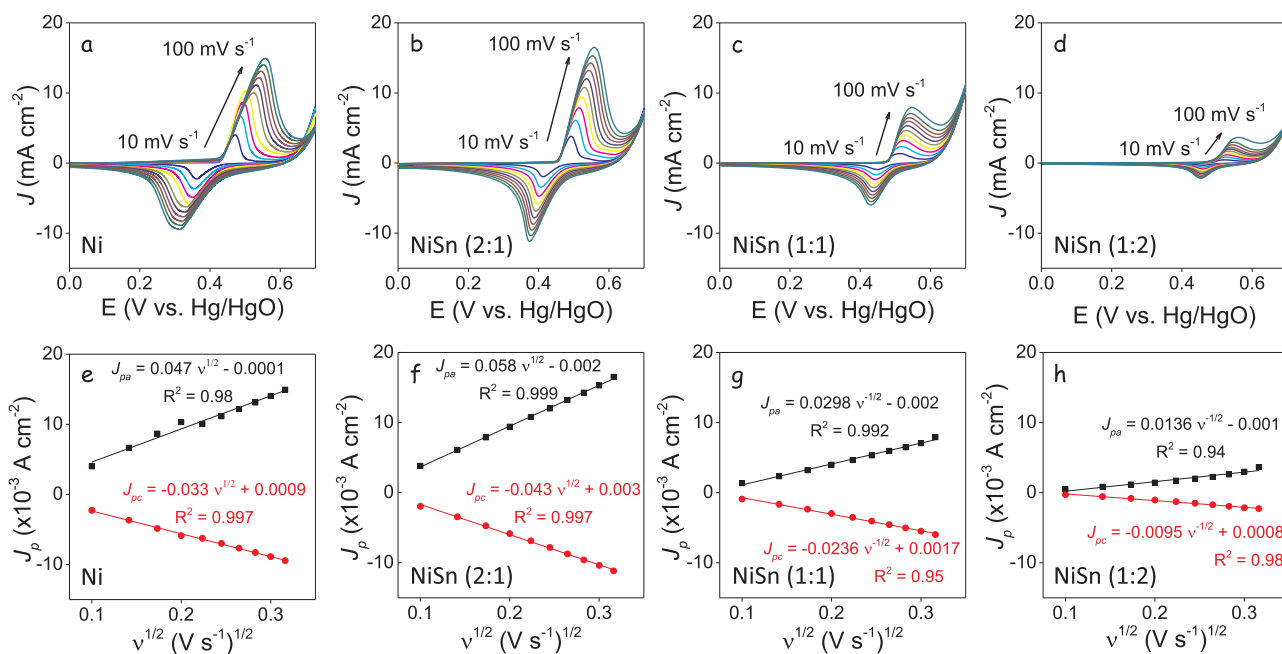


Fig. 6. (a–d) Cyclic voltammograms of Ni and NiSn electrocatalysts in 0.50 KOH at increasingly higher potentials sweep rates: 10, 20, 30, 40, 50, 60, 70, 80, 90, 100 mV s⁻¹. (e–h) Linear fitting of the anodic and cathodic peak current densities to the square roots of the scan rates.

Table 2

Summary of the electrocatalytic performance.

Catalyst	J_{pa} mA cm ⁻²	J_{pc} mA cm ⁻²	$E_{1/2}$ V vs Hg/HgO	ΔE_p V	Γ mol cm ⁻²	D cm ² s ⁻¹
Ni	10.5	-6.8	0.47	0.190	2.5×10^{-7}	1.2×10^{-11}
NiSn (2:1)	10.8	-6.9	0.49	0.139	2.1×10^{-7}	1.9×10^{-11}
NiSn (1:1)	4.7	-3.5	0.50	0.090	1.1×10^{-7}	5.3×10^{-12}
NiSn (1:2)	1.7	-1.3	0.51	0.076	4.5×10^{-8}	1.0×10^{-13}

parameters constant, but removing OAc, large spherical aggregates of NiSn NPs with the Ni₃Sn₄ crystal phase were produced (Fig. S1). On the other hand, in the absence of TOP, NiSn NPs aggregated in chains and with the Ni₃Sn₄ crystal phase were obtained (Fig. S2).

However, the presence of organic ligands at the NP surface strongly limits both their ability to interact with the media and the charge transport between NPs and between NPs and surrounding materials. Thus, we removed the native organic ligands from the NiSn NP surface by suspending them in a mixture of acetonitrile and a small amount of hydrazine hydrate. The mixture was stirred for some hours and then the precipitated NPs were collected. Additional purification steps with acetonitrile were carried out to remove all the unbounded or loosely

bond organics. FTIR analysis confirmed the absence of organic ligands at the NiSn NP surface after the ligand removal step, as observed from the disappearing of peaks at 2890 cm⁻¹ and 2822 cm⁻¹ that correspond to C–H stretching modes (Fig. 4).

Electrocatalysts were prepared by mixing NPs with CB and Nafion and supporting this composite onto a glassy carbon electrode (see experimental section for details). As reference materials, 12 nm Ni NPs and 13 nm Sn NPs produced following previously published synthetic routes (see experimental section for details) were used. Figs. S6 and S7 display representative TEM micrographs and the corresponding XRD patterns of these reference materials. Surface ligands of these NPs were removed following the same procedure used to displace ligands from

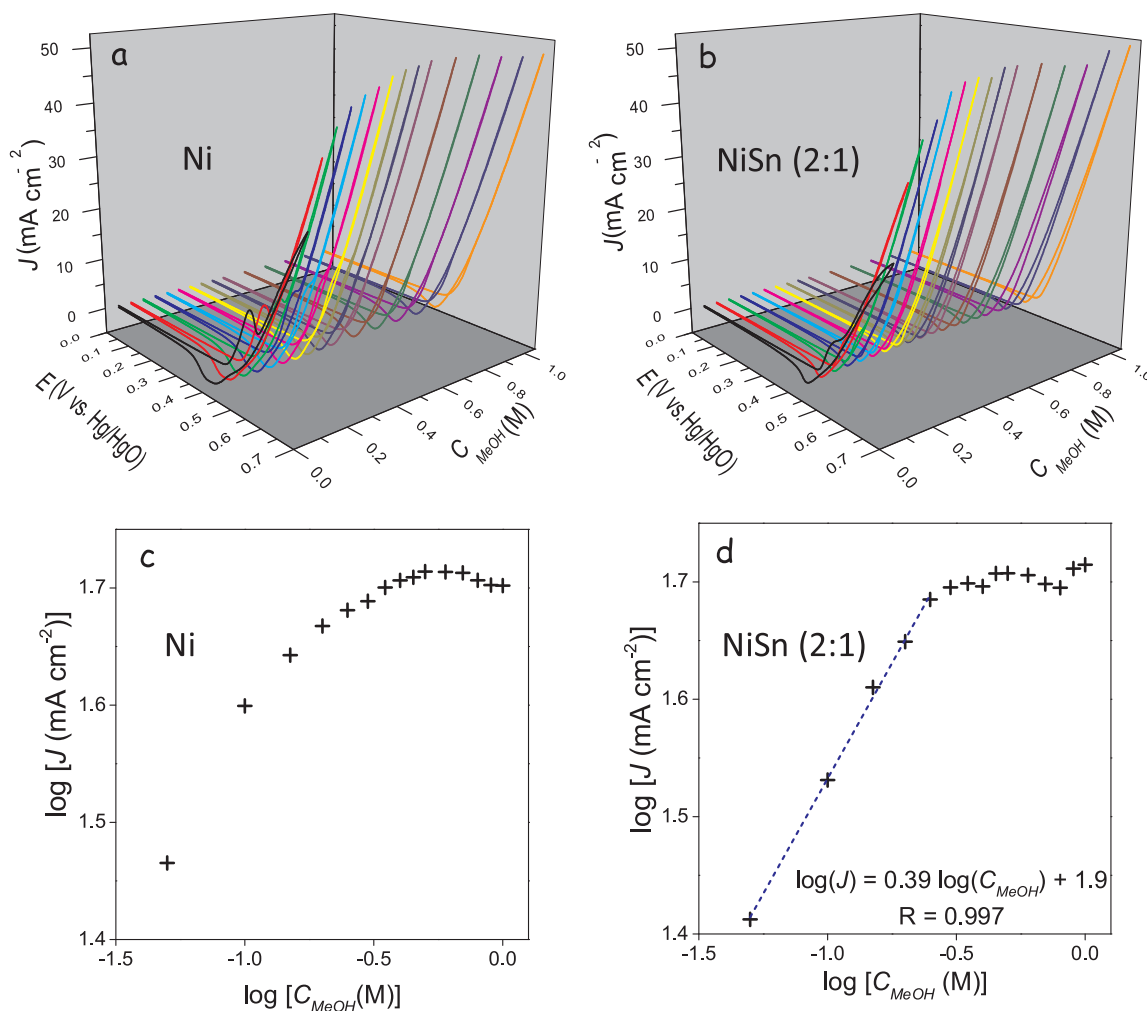


Fig. 7. Cyclic voltammograms (a,b) and logarithmic dependence of the current density (0.70 V vs Hg/HgO) with the methanol concentration (c,d) for a Ni electrode (a,c) and a NiSn (2:1) electrode (b,d) in 0.50 M KOH solution with various methanol concentrations from 0.05 M to 1.00 M at a scan rate of 50 mV s⁻¹.

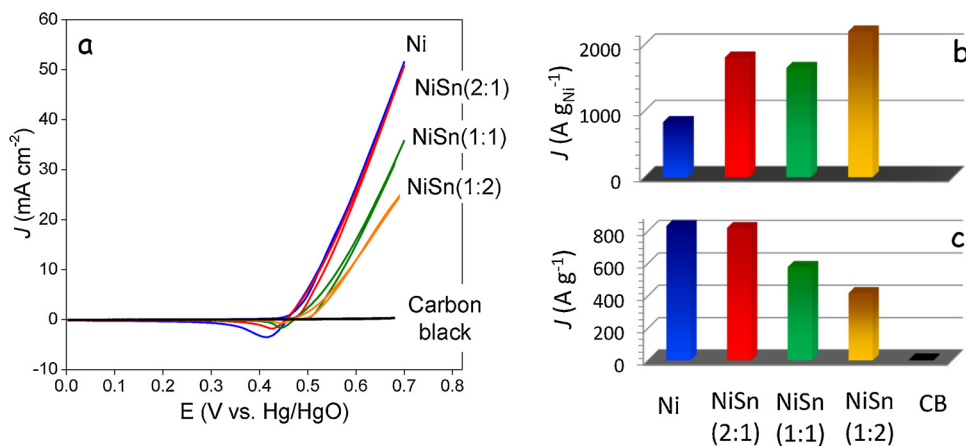


Fig. 8. (a) Cyclic voltammograms of CB, Ni, and NiSn-based electrodes in 0.50 M KOH with 0.50 M methanol at a sweep rate of 50 mV s⁻¹. (b) Mass current densities considering only the mass of Ni for Ni, and NiSn-based electrodes in 0.50 M KOH containing 0.50 M methanol at 0.70 V vs. Hg/HgO. (c) Mass current densities for CB, Ni, and NiSn-based electrodes in the same solution and at the same voltage.

NiSn NPs.

The electrocatalytic activity toward the MOR of NiSn NPs with different compositions was initially tested using cyclic voltammetry. Fig. 5 presents cyclic voltammograms of the five different electrocatalysts tested in 0.50 M KOH medium without (Fig. 5a) or with (Fig. 5b) 0.50 M methanol. The scan rate was set at 50 mV s⁻¹ and the potential window measured extended from 0 V to 1.0 V vs Hg/HgO. Cyclic voltammograms in the absence of methanol were conducted to determine the potential range for Ni oxidation and oxygen evolution

from water (OER).

The anodic oxidation of nickel in alkaline media has been extensively investigated. It is generally accepted that in alkaline medium, Ni undergoes oxidation to Ni(OH)₂ [11,30–32]. In the absence of methanol, for the Ni electrocatalyst, we measured the first anodic peak at ca. 0.50 V vs Hg/HgO and ascribed it to the oxidation of Ni(OH)₂ to NiOOH. Still during the forward scan, a second increase in the current density at 0.75 V vs Hg/HgO was attributed to OER. Subsequently, the formed NiOOH was reduced in the backward direction at a potential

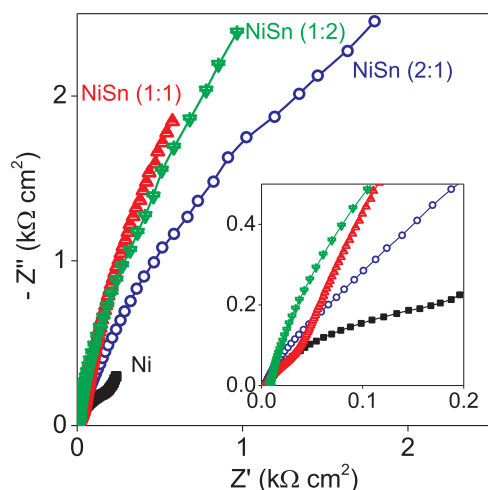


Fig. 9. Nyquist plot of the methanol oxidation on Ni- and NiSn-based electrodes in a 0.50 M KOH + 0.50 M methanol solution at 0.70 V vs Hg/HgO.

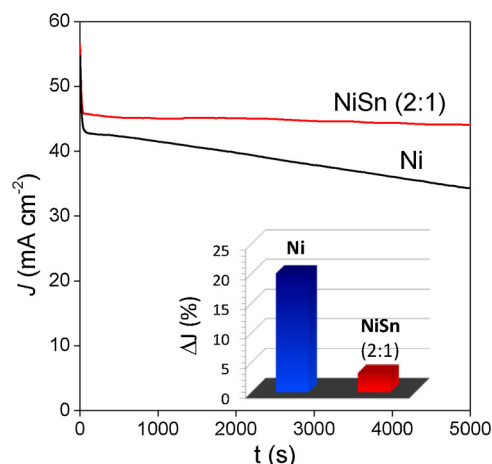
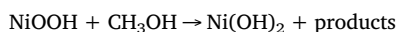
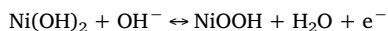


Fig. 10. Chronoamperometry of NiSn (2:1) and Ni electrodes at 0.70 V vs. Hg/HgO in 0.50 M KOH containing 0.50 M methanol.

value of ca. 0.50 V vs Hg/HgO.

Using NiSn bimetallic NPs, the current densities of the first anodic and cathodic peaks decreased as the Sn content increased (Fig. 5a). The current densities at the first oxidation peak were 10.5 mA cm^{-2} for Ni, 10.8 mA cm^{-2} for NiSn (2:1), 4.7 mA cm^{-2} for NiSn (1:1) and 1.7 mA cm^{-2} for NiSn (1:2) electrodes. In parallel, the corresponding oxidation and reduction onset potentials shifted with increasing Sn contents. The onset oxidation potential of Ni was 0.468 V vs Hg/HgO and that of NiSn was 0.482 V, 0.483 V and 0.516 V for (2:1), (1:1) and (1:2) compositions, respectively. Sn electrodes displayed no redox peaks in the measured potential window and showed an OER activity comparable to that of carbon black. Consistently, in spite of the non-homogeneous Ni and Sn distribution within each particle, only one oxidation and reduction peak was observed for each sample.

Fig. 5b shows cyclic voltammograms measured in the presence of methanol. The MOR onset was at ca. 0.43 V vs Hg/HgO, the same voltage at which Ni(OH)_2 undergoes oxidation to NiOOH. This is consistent with the proposed mechanisms of electrocatalytic MOR on Ni-based anodes, which involves the participation of the nickel oxyhydroxide in the methanol oxidation [9,18,33]:



with carbonate, formaldehyde, formic acid, CO, and CO_2 as the

possible products/intermediates of the MOR. Notice also in this direction, that the cathode peak, associated to the reduction of NiOOH to Ni(OH)_2 decreased or fully disappeared with the introduction of the MOR, confirming the consumption of this compound during the MOR.

Fig. 5b shows how the activity toward the MOR of the NiSn electrodes decreased with the amount of Sn. The activity of the Sn electrode was very low, confirming that elemental Sn did not catalyze the OER and MOR reactions in the voltage range studied. Activity of NiSn electrocatalysts was generally lower than that of Ni, except for the NiSn with the higher Ni content (2:1), which provided higher current densities up to a certain voltage when the OER reaction kicked in. In this regard, note also that MOR and OER reactions occurred simultaneously at voltages above 0.75 V. Thus, to further test the activity toward MOR without influence of the OER, we limited the analyzed potential to the range from 0 to 0.70 V vs Hg/HgO.

Fig. 6 displays the cyclic voltammograms in the 0 V–0.70 V vs Hg/HgO range and at various scan rates of the Ni and NiSn electrodes within 0.50 KOH media and with no methanol. The anodic and cathodic peaks increased and shifted to higher and lower potentials respectively when increasing the scan rate. For all electrocatalysts, the ratio of the current densities at the anodic and cathodic peaks indicated the nickel redox reaction to be mostly reversible.

To quantify the redox $\text{Ni(OH)}_2 \leftrightarrow \text{NiOOH}$ reaction, the peak anodic (J_{pa}) and cathodic (J_{pc}) current densities, the half wave redox potential ($E_{1/2}$), the redox potential difference (ΔE_p), the NiOOH surface coverage (Γ) and the proton diffusion coefficient (D), of the different electrocatalysts tested were determined (Table 2). Peak current densities were higher for NiSn (2:1) than for Ni-based electrodes, but decreased with the Sn content. Sharper oxidation and reduction peaks were obtained for all the NiSn-based electrodes compared with Ni, which could be related to the smaller size of the NiSn NPs. While $E_{1/2}$ increased with the Sn content, ΔE_p decreased with the incorporation of Sn, suggesting faster electron transfer kinetics. The surface coverage of $\text{Ni(OH)}_2/\text{NiOOH}$ redox pairs participating in the reaction at each Ni-Sn electrode was calculated using the following equation [34,35]:

$$\Gamma = \frac{Q}{nFA}$$

where Q is the charge under the reduction/oxidation peak, which we averaged from forward and reverse scans, A is the geometrical electrode surface area, n is the number of transferred electron per reaction, i.e. 1, and F is the Faraday constant.

The calculated NiOOH surface coverages were independent of the scan rate in the low scan rate range ($v < 50 \text{ mV s}^{-1}$). The coverage of electroactive species decreased as the amount of Sn in the NiSn NPs increased (Table 2). However, the coverage obtained from NiSn (2:1) electrocatalysts was very close to that of Ni. This experimental result was at first view surprising taking into account the lower overall amount of metal in NiSn catalysts due to the higher atomic mass of Sn, the lower content of Ni in the NiSn NPs compared with elemental Ni NPs and the Sn-rich surface of NiSn NPs. However, it could be in part explained by the smaller size of the NiSn NPs compared with the Ni NPs. Overall, the surface coverages obtained from the Ni and NiSn electrodes in the present work were almost an order of magnitude higher than values usually reported, which we associated to the large surface area of the NPs used here.

In the high scan rate range, a linear relationship could be fitted to the dependence of the peak current density with the square root of the voltage scan rate, pointing toward a diffusion-limited $\text{Ni(OH)}_2 \leftrightarrow \text{NiOOH}$ redox reaction [30,36]. In this regard, it is generally accepted that the proton diffusion is the rate limiting step in the oxidation of Ni(OH)_2 to NiOOH. Therefore, the proton diffusion coefficient (D) can be determined from equation [34]:

$$I_p = 2.69 \times 10^5 n^{3/2} A D^{1/2} C v^{1/2}$$

where I_p is the peak current and C is the initial concentration of redox

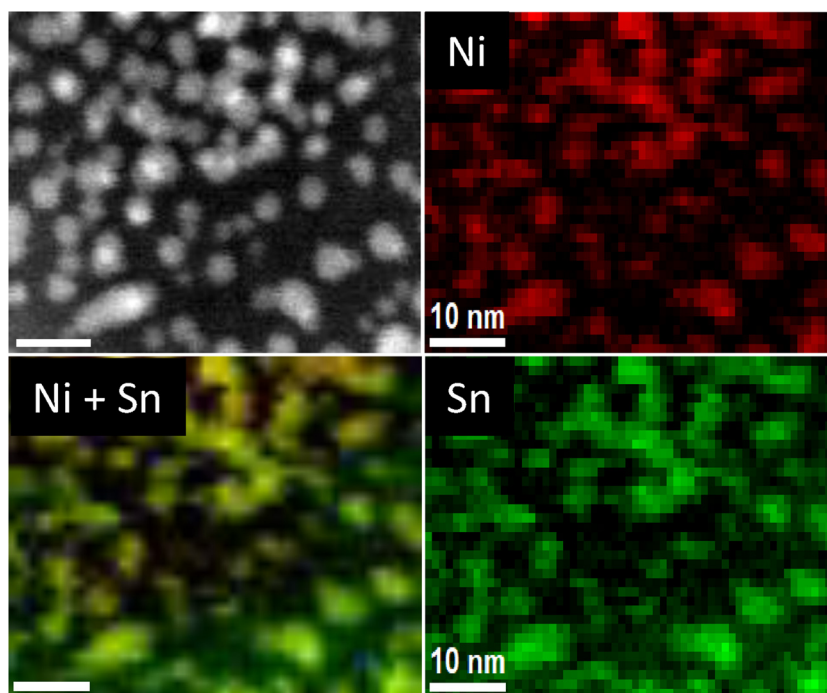


Fig. 11. EELS chemical composition maps of a NiSn (2:1) electrocatalyst after 10000s CA stability test: Individual Ni $L_{2,3}$ -edges at 855 eV (red), Sn $M_{4,5}$ -edges at 485 eV (green) and composite Ni-Sn map (For interpretation of the references to colour in this figure legend, the reader is referred to the web version of this article).

species that, taking into account a $\text{Ni}(\text{OH})_2$ density of 3.97 g cm^{-3} , we estimated at $0.043 \text{ mol cm}^{-3}$.

The proton diffusion coefficient obtained from Ni nanoparticles was $1.2 \times 10^{-11} \text{ cm}^2 \text{ s}^{-1}$, consistent with previous works [36]. Remarkably, the diffusion coefficient for NiSn (2:1) was slightly higher, $1.9 \times 10^{-11} \text{ cm}^2 \text{ s}^{-1}$, but as Sn concentration increased, this apparent diffusion coefficient decreased (Table 2).

Fig. 7a–b displays cyclic voltammograms (50 mV s^{-1}) of the Ni and the NiSn (2:1) electrocatalysts in a media containing different methanol concentrations, from 0.05 M to 1.00 M. It can be observed that the Ni $(\text{OH})_2$ oxidation peak gradually disappears within the large current density increase related to the MOR when the methanol concentration increases. Fig. 7c–d displays the dependence of the current density measured at 0.70 V vs Hg/HgO with the methanol concentration. The current density at 0.70 V vs Hg/HgO rapidly increased in the low methanol concentration range and stabilized at methanol concentrations around 0.30 M. A linear fit of the logarithmic plot of the current density of MOR versus the methanol concentration for the NiSn (2:1) electrode pointed toward an apparent methanol reaction order of around 0.4. A similar reaction order was obtained for all NiSn-based electrodes (Fig. S8). No clear linear relationship could be fitted to the Ni electrode (Fig. 7c).

While saturating at relatively low methanol concentrations, very high current densities and mass current densities were obtained for Ni and NiSn NP-based electrodes (Figs. 7, 8 and S9). Fig. 8a displays the cyclic voltammograms of the electrocatalysts based on Ni NPs, Sn NPs, CB, and Ni-Sn NPs in 0.50 M KOH with 0.50 M methanol. Mass current densities were calculated taking into account the mass of metal in each electrode (Fig. 8c). The calculated mass current density was 830 A g^{-1} for Ni and 820 A g^{-1} for NiSn (2:1)-based electrodes. When we increase the amount of Sn, the mass current densities decreased to 580 A g^{-1} and 420 A g^{-1} for NiSn (1:1) and NiSn (1:2), respectively. When only considering the mass of Ni as the active element to evaluate the mass current density (Fig. 8b), all NiSn NP-based electrodes showed similar performances, all much higher than that of elemental Ni NPs: 830 A g^{-1} for Ni, $1800 \text{ A g}_{\text{Ni}}^{-1}$ for NiSn (2:1), $1650 \text{ A g}_{\text{Ni}}^{-1}$ for NiSn (1:1) and $2250 \text{ A g}_{\text{Ni}}^{-1}$ for NiSn (1:2). A comparison of catalytic performance

between our results and previously reported Ni-based catalysts towards MOR is listed in Table S1. From this comparison, we conclude that NiSn NPs are excellent candidates for the electro-oxidation of methanol in alkaline medium.

Fig. 9 displays the Nyquist plot of the impedance spectra of methanol oxidation on Ni, NiSn (2:1), NiSn (1:1) and NiSn (1:2) electrodes. The measurements were made in a 0.50 M KOH + 0.50 M methanol solution at 0.70 V vs Hg/HgO. We observed the impedance associated to the charge transfer for methanol electrochemical oxidation to increase with the amount of Sn.

Chronoamperometric measurements were used to determine the electrocatalysts stability. Fig. 10 shows the chronoamperograms of NiSn (2:1) and Ni electrodes in a 0.50 M KOH solution containing 0.50 M methanol at 0.70 V vs Hg/HgO. The current densities largely dropped in the first minutes and then relatively stabilized. Similarly fast initial drops were previously observed [14] and are generally attributed to the fact that initially active sites are free of adsorbed methanol molecules and no methanol depletion layer around the electrode exist, allowing a very fast initial reaction. In the first minutes, an equilibrium coverage of methanol at the catalyst surface and an equilibrium gradient of methanol around the electrode are established, dropping the current density to a lower value. The posterior progressive drop of current density is most likely related to the poisoning of the active sites at the electrode with reaction products. Fig. S10 displays the chronoamperograms obtained from the different electrodes in a magnetically stirred 0.50 M KOH solution containing 0.50 M methanol at 0.70 V vs Hg/HgO. In this case, no methanol depletion layer is formed and current densities do not suffer any initial drop. On the contrary, they increased in the first minutes to later decrease over the 10,000 s studied.

Fig. 11 shows a representative STEM micrograph of the NiSn (2:1) electrocatalyst after a 10,000 s stability test. A broader size distribution of the NCs was observed, which could be related to a partial aggregation during electrocatalyst formulation. In the same figure, the EELS chemical compositional maps of the NPs are displayed. While signal and resolution were not optimal due to the presence of the electrocatalyst additives, i.e. CB and Nafion, compositional maps showed the existence of Ni and Sn in all the nanoparticles and no clear phase

segregation could be identified.

Overall, NiSn-based electrodes clearly displayed improved stabilities over Ni-based electrocatalysts. This experimental fact could have two different explanations: (i) The presence of Sn can contribute to the oxidation of the MOR products that poisons the Ni surface sites. In this direction, lattice or adsorbed oxygen or OH[−] groups on Sn metal, oxide or hydroxide could further oxidize MOR products that strongly adsorb onto the Ni sites poisoning its surface. (ii) Alternatively, the presence of Sn atoms within the Ni structure, forming a Ni₃Sn₂ phase, certainly modifies the electronic density of states of Ni, thus affecting its chemistry, which could prevent strong binding of particular poisoning species. Additional work would be required to exactly assess the mechanism of improvement of the electrode stability with the Sn incorporation.

4. Conclusion

In summary, a new synthetic route to produce NiSn intermetallic NPs with composition control was developed. Detailed electrochemical measurements showed that these NPs exhibited excellent performance for MOR in alkaline solution. Ni-rich NiSn-based electrocatalysts displayed slightly improved performances than Ni-based electrocatalysts. Most notorious was the significantly improved stability of NiSn catalysts compared with that of Ni. This work represents a significant advance in developing cost-effective electrocatalysts with high activity and stability for MOR in DMFCs.

Conflict of interest

The authors declare no competing financial interest.

Acknowledgments

J. Li and T. Zhang thank the China Scholarship Council for scholarship support. JA and TZ acknowledge funding from Generalitat de Catalunya 2014 SGR 1638 and the Spanish MINECO coordinated projects between IREC and ICN2 VALPEC and subprojects RESOL and ANAPHASE (ENE2017-85087-C3). ICN2 acknowledges support from the Severo Ochoa Programme (MINECO, Grant no. SEV-2013-0295) and is funded by the CERCA Programme / Generalitat de Catalunya. JL is a Serra Hùnter Fellow and is grateful to ICREA Academia program and to MINECO/FEDER grant ENE2015-63969-R.

Appendix A. Supplementary data

Supplementary material related to this article can be found, in the online version, at doi:<https://doi.org/10.1016/j.apcatb.2018.04.017>.

References

- [1] M. Sgroi, F. Zedde, O. Barbera, A. Stassi, D. Sebastián, F. Lufano, V. Baglio, A. Aricò, J. Bonde, M. Schuster, Cost analysis of direct methanol fuel cell stacks for mass production, *Energies* 9 (2016) 1008.
- [2] T. Schultz, S. Zhou, K. Sundmacher, Current status of and recent developments in the direct methanol fuel cell, *Chem. Eng. Technol.* 24 (2001) 1223–1233.
- [3] S.S. Munjewar, S.B. Thombre, R.K. Mallick, A comprehensive review on recent material development of passive direct methanol fuel cell, *Ionics (Kiel)* 23 (2017) 1–18.
- [4] P. Kumar, K. Dutta, S. Das, P.P. Kundu, An overview of unsolved deficiencies of direct methanol fuel cell technology: factors and parameters affecting its widespread use, *Int. J. Energy Res.* 38 (2014) 1367–1390.
- [5] Z. Dağdelen, Y. Yıldız, S. Eriş, F. Şen, Enhanced electrocatalytic activity and durability of Pt nanoparticles decorated on GO-PVP hybriide material for methanol oxidation reaction, *Appl. Catal. B Environ.* 219 (2017) 511–516.
- [6] G. Long, X. Li, K. Wan, Z. Liang, J. Piao, P. Tsiakaras, Pt/CN-doped electrocatalysts: superior electrocatalytic activity for methanol oxidation reaction and mechanistic insight into interfacial enhancement, *Appl. Catal. B Environ.* 203 (2017) 541–548.
- [7] M.A. Abdel Rahim, R.M. Abdel Hameed, M.W. Khalil, Nickel as a catalyst for the electro-oxidation of methanol in alkaline medium, *J. Power Sources* 134 (2004) 160–169.
- [8] M. Zhou, P. Xiao, W. Guo, J. Deng, F. Liu, Y. Zhang, Electrochemical synthesis of monodisperse nickel with predominant orientation and High electro-oxidation activity for methanol, *J. Electrochem. Soc.* 161 (2014) H133–H137.
- [9] R.M. Abdel Hameed, R.M. El-Sherif, Microwave irradiated nickel nanoparticles on Vulcan XC-72R carbon black for methanol oxidation reaction in KOH solution, *Appl. Catal. B Environ.* 162 (2015) 217–226.
- [10] M.W. Khalil, M.A. Abdel Rahim, A. Zimmer, H.B. Hassan, R.M. Abdel Hameed, Nickel impregnated silicalite-1 as an electro-catalyst for methanol oxidation, *J. Power Sources* 144 (2005) 35–41.
- [11] D. Wu, W. Zhang, D. Cheng, Facile synthesis of Cu/NiCu electrocatalysts integrating alloy, core-shell, and one-dimensional structures for efficient methanol oxidation reaction, *ACS Appl. Mater. Interfaces* 9 (2017) 19843–19851.
- [12] I. Danaee, M. Jafarian, F. Forouzandeh, F. Gopal, M.G. Mahjani, Electrocatalytic oxidation of methanol on Ni and NiCu alloy modified glassy carbon electrode, *Int. J. Hydrogen Energy* 33 (2008) 4367–4376.
- [13] R. Ding, J. Liu, J. Jiang, F. Wu, J. Zhu, X. Huang, Tailored Ni–Cu alloy hierarchical porous nanowire as a potential efficient catalyst for DMFCs, *Catal. Sci. Technol.* 1 (2011) 1406.
- [14] X. Cui, P. Xiao, J. Wang, M. Zhou, W. Guo, Y. Yang, Y. He, Z. Wang, Y. Yang, Y. Zhang, Z. Lin, Highly branched metal alloy networks with superior activities for the methanol oxidation reaction, *Angew. Chem. Int. Ed.* 56 (2017) 4488–4493.
- [15] S.L. Candelaria, N.M. Bedford, T.J. Woehl, N.S. Rentz, A.R. Showalter, S. Pylypenko, B.A. Bunker, S. Lee, B. Reinhart, Y. Ren, S.P. Ertem, E.B. Coughlin, N.A. Sather, J.L. Horan, A.M. Herring, L.F. Greenlee, Multi-component Fe–Ni hydroxide nanocatalyst for oxygen evolution and methanol oxidation reactions under alkaline conditions, *ACS Catal.* 7 (2017) 365–379.
- [16] X. Cui, W. Guo, M. Zhou, Y. Yang, Y. Li, P. Xiao, Y. Zhang, X. Zhang, Promoting effect of Co in Ni_mCo_n (m + n = 4) bimetallic electrocatalysts for methanol oxidation reaction, *ACS Appl. Mater. Interfaces* 7 (2015) 493–503.
- [17] I. Danaee, M. Jafarian, A. Mirzapoor, F. Gopal, M.G. Mahjani, Electrooxidation of methanol on NiMn alloy modified graphite electrode, *Electrochim. Acta* 55 (2010) 2093–2100.
- [18] Q. Yi, W. Huang, J. Zhang, X. Liu, L. Li, Methanol oxidation on titanium-supported nano-scale Ni flakes, *Catal. Commun.* 9 (2008) 2053–2058.
- [19] Y. Yu, Q. Yang, X. Li, M. Guo, J. Hu, A bimetallic Ni–Ti nanoparticle modified indium tin oxide electrode fabricated by the ion implantation method for studying the direct electrocatalytic oxidation of methanol, *Green Chem.* 18 (2016) 2827–2833.
- [20] Y. Wang, X. Wang, Y. Wang, J. Li, Acid-treatment-assisted synthesis of Pt–Sn/graphene catalysts and their enhanced ethanol electro-catalytic activity, *Int. J. Hydrogen Energy* 40 (2015) 990–997.
- [21] X. Wang, J. Lian, Y. Wang, The effect of Sn on platinum dispersion in Pt/graphene catalysts for the methanol oxidation reaction, *Int. J. Hydrogen Energy* 39 (2014) 14288–14295.
- [22] D.-H. Lim, D.-H. Choi, W.-D. Lee, D.-R. Park, H.-I. Lee, The effect of Sn addition on a Pt/C electrocatalyst synthesized by borohydride reduction and hydrothermal treatment for a low-temperature fuel cell, *Electrochem. Solid-State Lett.* 10 (2007) B87.
- [23] J. Liu, Y. Wen, P.A. van Aken, J. Maier, Y. Yu, Facile synthesis of highly porous Ni–Sn intermetallic microcages with excellent electrochemical performance for lithium and sodium storage, *Nano Lett.* 14 (2014) 6387–6392.
- [24] Y. Liu, X. Liu, Q. Feng, D. He, L. Zhang, C. Lian, R. Shen, G. Zhao, Y. Ji, D. Wang, G. Zhou, Y. Li, Intermetallic Ni_xM_y (M = Ga and Sn) nanocrystals: a non-precious metal catalyst for semi-hydrogenation of alkynes, *Adv. Mater.* 28 (2016) 4747–4754.
- [25] K. Kravchuk, L. Protesescu, M.I. Bodnarchuk, F. Krumeich, M. Yarema, M. Walter, C. Guntlin, M.V. Kovalenko, Monodisperse and inorganically capped Sn and Sn/SnO₂ nanocrystals for high-performance Li-ion battery anodes, *J. Am. Chem. Soc.* 135 (2013) 4199–4202.
- [26] Y. Chen, X. Luo, H. She, G.-H. Yue, D.-L. Peng, Size- and structure-controlled synthesis and characterization of nickel nanoparticles, *J. Nanosci. Nanotechnol.* 9 (2009) 5157–5163.
- [27] A. Yakymovych, H. Ipsen, Synthesis and characterization of pure Ni and Ni–Sn intermetallic nanoparticles, *Nanoscale Res. Lett.* 12 (2017) 142.
- [28] C. Schmetterer, H. Flandorfer, K.W. Richter, U. Saeed, M. Kauffman, P. Roussel, H. Ipsen, A new investigation of the system Ni–Sn, *Intermetallics* 15 (2007) 869–884.
- [29] C.D. Wager, W.M. Riggs, L.E. Davis, J.F. Moulder, G.E. Muilenderg, Handbook of X-ray Photoelectron Spectroscopy, Perkin-Elmer Corporation Physical Electronics Division, 1979.
- [30] D.M. MacArthur, The hydrated nickel hydroxide electrode potential sweep experiments, *J. Electrochem. Soc.* 117 (1970) 422.
- [31] P. Oliva, J. Leonardi, J.F. Laurent, C. Delmas, J.J. Braconnier, M. Figlarz, F. Fievet, Ad. Guibert, Review of the structure and the electrochemistry of nickel hydroxides and oxy-hydroxides, *J. Power Sources* 8 (1982) 229–255.
- [32] Z. Jiang, Y. Xiang, J. Wang, Study of the oxidation layer on the nickel surface in 1 M NaOH solution using the in-situ photothermal spectroscopy method, *J. Electroanal. Chem. Interfacial Electrochem.* 316 (1991) 199–209.
- [33] N.A.M. Barakat, M. Motlak, CoxNiy-decorated graphene as novel, stable and super effective non-precious electro-catalyst for methanol oxidation, *Appl. Catal. B Environ.* 154 (2014) 221–231.
- [34] A.J. Bard, L.R. Faulkner, *Electrochemical Methods Fundamentals and Applications*, (2001).
- [35] D. Chen, S.D. Minter, Mechanistic study of nickel based catalysts for oxygen evolution and methanol oxidation in alkaline medium, *J. Power Sources* 284 (2015) 27–37.
- [36] C. Zhang, S. Park, The anodic oxidation of nickel in alkaline media studied by spectroelectrochemical techniques, *J. Electrochem. Soc.* 134 (1987) 2966.